ROYAL SOCIETY OF CHEMISTRY

www.rsc.org/faraday_d

Nonlinear Ion Transport in a 2D Janus Membrane with an Angstrom Pore: Memristive and Negative Differential Resistance Phenomena

Mohan Teja Dronadula[a] and Narayana R. Aluru[b]*

[a] Walker Department of Mechanical Engineering, The University of Texas at Austin, Austin, Texas 78712, USA.

[b] Oden Institute for Computational Engineering and sciences, The University of Texas at Austin, Austin, Texas 78712, USA.

Abstract

We report nanofluidic memristive behavior and negative differential resistance (NDR) in a MoSSe angstrom pore using molecular dynamics (MD) simulations. The system exhibits pinched-loop hysteresis in its current-electric field (*I-E*) response when subjected to a sinusoidal electric field pulse. Furthermore, we identified a NDR region, marked by a conductance switch from low to high resistance beyond a critical threshold electric field. This switching behavior originates from electric field induced dipole ordering of water confined within the nanopore, leading to an increased translocation barrier. We further show that the system exhibits biological synapse like behavior, exhibiting neuromorphic functions such as short-term plasticity and paired-pulse facilitation/depression. These findings demonstrate that nanoscale confined solvent ordering can serve as a physical basis for achieving non-linear ion transport behavior, enabling applications in next-generation neuromorphic computing systems.

Keywords: Nanofluidic memristors, Negative Differential Resistance, Molecular Dynamics, Angstrom Pores, Short-term Plasticity, Neuromorphic Computing.

----

*corresponding author, email: aluru@utexas.edu, web: https://sites.utexas.edu/aluru/

1. Introduction

Synapses are specialized connections between neurons in biological neural networks that enable the transmission, modulation and storage of information. These connections are inherently plastic, a property that underlies the brain's capacity for learning and adaptation[1]. Synapses achieve this by adjusting their efficacy (which acts as an internal state variable) based on the history of neural activity, thus embodying past inputs as memory. Through this dynamic, activity-dependent plasticity, synapses simultaneously encode prior activity and process new signals, serving as the fundamental substrate for both information storage and computation in the brain.

Memristors have emerged as novel electronic components capable of emulating this coupled memory-computation behavior of biological synapses. Their appeal lies in unifying processing and storage within a single element, thereby overcoming the von Neumann bottleneck[2]. The concept was first theorized by Leon Chua in 1971[3] as the missing fourth fundamental circuit element that relates electric charge with magnetic flux. It was later realized experimentally[4] in 2008. Since then, numerous studies have investigated solid-state memristors based on modulating electron/hole transport using various phenomena[4–8]. More recently, attention has shifted toward nanofluidic memristors, with several studies demonstrating their operation through a range of nanoscale phenomena, including ion induced distortion of solvent ordering or networking[9], electrowetting[10], concentration polarization[11,12], ion adsorption/desorption[13,14], the Wien effect[15,16], electrostriction[17], etc. These systems function analogously to their electronic counterparts but utilize ions rather than electrons, allowing operation at lower voltages and reduced power consumption[13,18]. When driven by signals on timescales comparable to the relaxation timescales of the underlying processes, they exhibit pinched hysteresis loops (a hallmark of memristors) and activity-dependent plasticity reminiscent of biological neurons.

Beyond such memristive hysteresis, another important nonlinear ion transport behavior is negative differential resistance (NDR), in which an increase in applied voltage produces a decrease in current over a finite bias range. This characteristic plays a crucial role in circuit implementations of the FitzHugh-Nagumo (FN) neuron model[19,20], where it provides the nonlinear element required for generating excitability and spike-like dynamics observed in neurons. Numerous solid state NDR memristors have been demonstrated and successfully employed to emulate such spiking behavior[20–24], whereas only a few nanofluidic systems have exhibited such capabilities[14,25,26].

In this study, we present a nanofluidic NDR memristor based on angstrom pores in Janus MoSSe membrane. By applying a sinusoidal electric field across the membrane, we observe pinched loop hysteresis together with NDR. We investigate the mechanism underlying these behaviors and find that the electric field induces a pronounced alignment of water dipoles inside the nanopore. We show that the dipole orientation strengthens with electric field, and the

translocation barrier for ions correspondingly increases, leading to a reduction in current and the emergence of NDR. We also explain that in the reverse sweep, due to the longer timescale associated with the relaxation of the dipole-oriented water structure compared to forward process, the system retains a more ordered state, resulting in lower currents during the reverse sweep compared to the forward sweep. We further demonstrate biological neuron like short-term plasticity, exhibiting both short-term facilitation (STF) and short-term depression (STD). Paired-pulse facilitation (PPF) and paired-pulse depression (PPD) are also observed, allowing us to extract the characteristic memory timescales exhibited by our system. Additionally, current voltage curves obtained for different membrane charge states show that the water ordering mediated mechanism persists even in uncharged systems. Overall, this study reveals a unique confined water ordering induced nonlinear ion transport, with promising implications for next generation iontronic neuromorphic computing devices.

2. Methods

The simulated system consists of two water reservoirs containing 1M KCl, placed on either side of a 5.2 x 5.07 nm^2 MoSSe membrane, as shown in Figure-1A. The membrane contains a single nanopore with a center-to-center diameter of 0.85nm (Figure-1A). After equilibrating the system for 10ns in NVT ensemble, we applied a series of ten sinusoidal electric field pulses, as illustrated in Figure-1A. Each pulse had an amplitude A = 1.2 V/nm and a frequency f = 200 MHz. All simulations were performed using the GROMACS[27–30] simulation package with a timestep of 1fs at 300K, employing a Nosé-Hoover[31,32] thermostat with a relaxation time of τ_r = 0.1ps. Short-range non-bonded interactions (Lennard-Jones and real-space Coulomb) were truncated at 1.2nm, while long-range electrostatics were treated using the particle-mesh Ewald (PME) method[33]. Water molecules were modelled using the SPC/E water model[34], and ion-ion interactions followed the Joung-Cheatham parameters[35]. Parameters for Mo and S were adopted from previous work[36], while Se parameters were taken from the CHARMM forcefield[37]. Cross interactions were derived using the Lorentz-Berthelot mixing rules. The atomic charges assigned to Mo, S, and Se in the MoSSe membrane were +1.06e, -0.61e, and -0.45e, respectively. For MoS$_2$, the charges were +1.18e for Mo and -0.59e for S. These values were obtained using Bader charge partitioning scheme[38]. The MoSSe charges closely match the values reported in a previous work[39], while the MoS$_2$ charges are consistent with those reported elsewhere[40]. It should be noted that the precise magnitude of atomic charges does not play a crucial role in NDR or hysteresis (discussed in the Results section) as both mechanisms persist, albeit to a varying degree depending on the charges used. Unless otherwise noted, all plots were obtained by

averaging over 10 independent ensembles, except the PPF/PPD and STF/STD results, which were averaged over 150 ensembles.
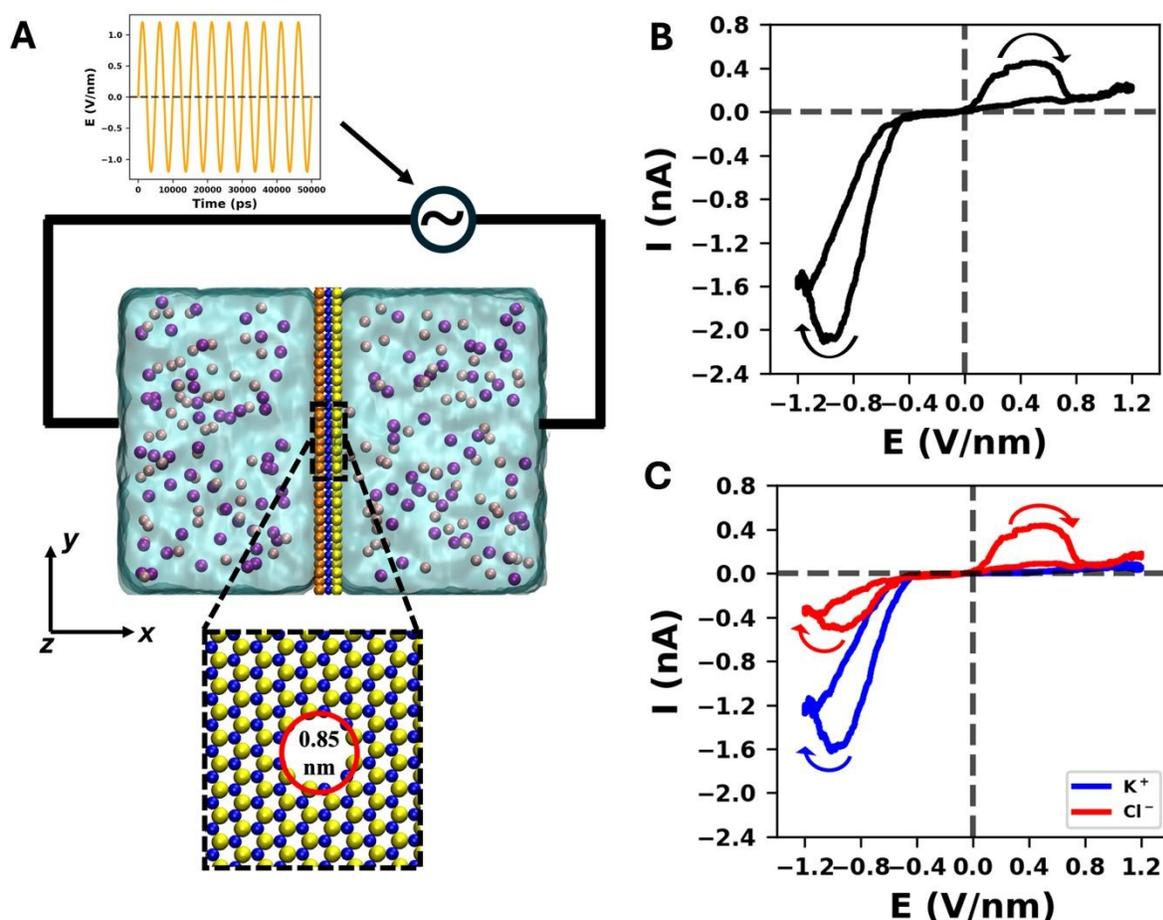
Figure 1 (A) Simulation set-up showing system, membrane, nanopore and electric field signal used. Here, Se, Mo and S atoms are represented by orange, blue and yellow spheres, respectively. (B) Current-electric field (*I-E*) characteristics. The arrow indicates the loop direction. (C) Decomposition of the total current in (B) into K$^+$ and Cl$^-$ contributions.

3. Results

3.1 Origin of Negative Differential Resistance

The current-electric field (*I-E*) response shown in Figure 1B exhibits NDR beyond $E = 0.5$ V/nm for positive electric fields and beyond $E = -1.0$ V/nm for negative electric fields. Furthermore, the *I-E* curve displays a pinched-loop hysteresis with unipolar memory features, where the reverse sweep currents are lower compared to forward sweep currents. Decomposition of the current into individual ionic (K$^+$ and Cl$^-$) contributions (Figure 1C) revealed that both ions exhibit similar features of NDR and hysteresis. To understand the mechanistic origin of the NDR

phenomenon, we investigated the Cl^- ion translocation energy barriers ($\Delta\omega$) as a function of electric field. These energy barriers are potential of mean force (PMF) barriers estimated as $\Delta\omega = -\int_{r_1}^{r_2}\langle F(x)\rangle dx$, where "$< F(x) >$" denotes the mean force, and r_1 and r_2 are the positions of the energy minima and maxima, respectively. Table 1 reports these energy barriers and their decompositions for different electric fields in the NDR region.

	water		membrane	total
	VdW	electrostatic		
0.3 V/nm (forward)	3.1	98.7	-75.52	19.3
0.5 V/nm (forward	4.3	108.8	-78.35	24
0.7 V/nm (forward)	5	126.2	-76.9	39.5

Table 1 Energy barriers and decompositions for Cl^- ions for different electric fields in the forward sweep. The energies are in kJ/mol. The total energy barriers also contain energy from applied external field.

The total energy barriers show a small increase from the 0.3V/nm to 0.5V/nm, and a more drastic increase from the 0.5V/nm to 0.7V/nm aligning with the NDR phenomenon. Further, the decompositions show that this increase in energy barriers causing NDR is primarily due to ion-water interactions, more specifically, electrostatic interactions. A similar phenomenon was previously reported for hydrophobic nanopores by Hansen et al.[41], where the application of an electric field increased the ion translocation energy barrier. This was explained to be caused by the electric field induced alignment of water dipoles producing an induced electric field that opposed ion motion. Upon inspecting the water structure inside the nanopore in our system, we noticed a similar phenomenon; the application of an electric field results in the water molecules inside the nanopore reorienting themselves such that their dipoles align parallel to the applied electric field, as shown in Figure 2A. Further, we quantified the extent of this alignment by projecting the dipole moment of each water molecule inside the nanopore onto the x-y plane and computing the angle between this projection and the x-axis (Figure 2A). We then calculated the probability distribution function of these angles and fit a Gaussian curve $P(\theta) = \frac{1}{\sqrt{2\pi\sigma_\theta^2}}e^{-\frac{(\theta-\mu)^2}{2\sigma_\theta^2}}$ to the distribution, where "μ" and "σ_θ" are the mean and standard deviation, respectively. Figure 2B shows these distributions for various electric fields in the forward and reverse sweeps and the standard deviations of these distributions are shown as a function of electric field in Figure 2C.
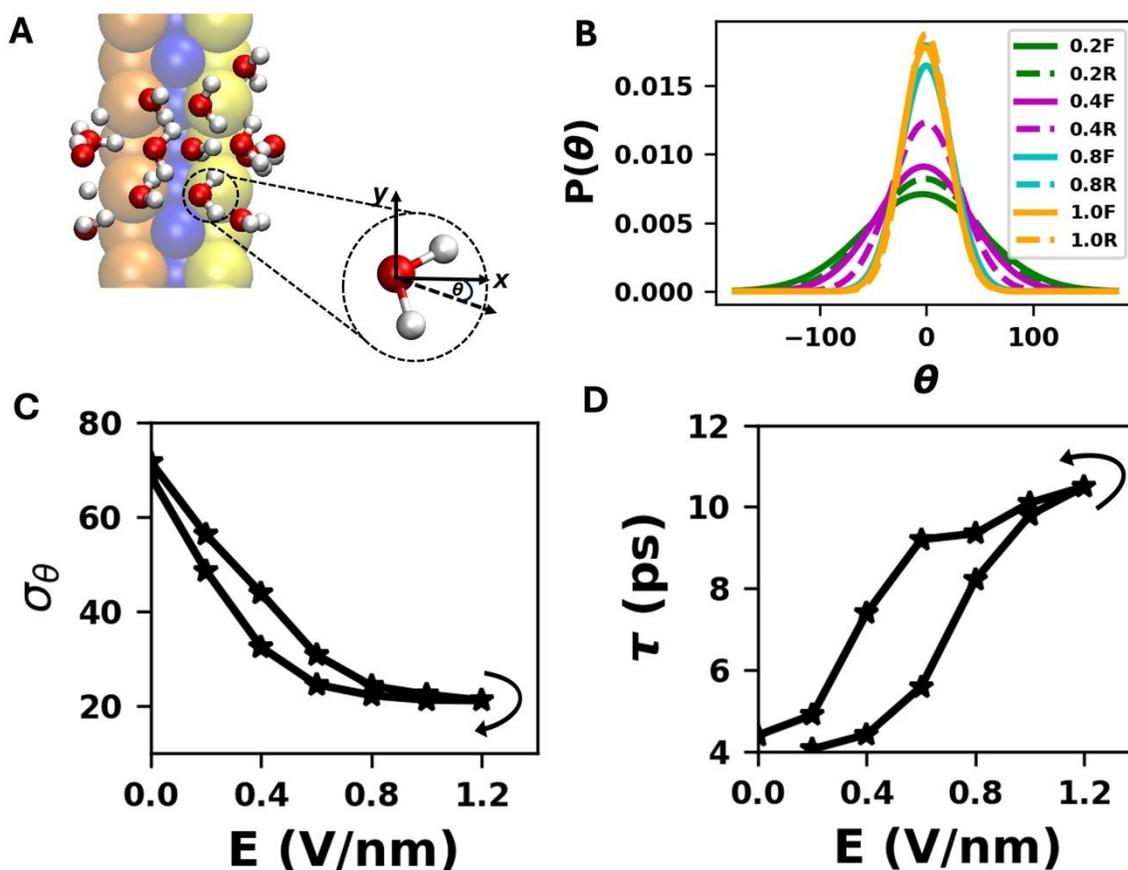
Figure 2 (A) Snapshot showing the nanopore with water molecules oriented parallel to applied field for positive electric fields. Here, the membrane is in the *y-z* plane with pore axis oriented along the *x*-axis and the field is applied in the positive *x*-direction, " θ " is the angle between the projection of the dipole in the *x-y* plane and the *x*-axis. (B) Distribution of water dipole orientation plots for various electric fields in the forward and reverse sweeps. (C) Standard deviation of water dipole orientation distributions vs electric field in the forward and reverse sweeps. (D) Water orientation relaxation times " τ " vs electric field in the forward and reverse sweeps.

Together, Figures 2B,C show that as the electric field increases during the forward sweep, the distributions become narrower (standard deviation reduces), indicating stronger orientation of the water molecules along the applied field. This stronger orientation would result in an induced electric field that acts against the applied field, thus impeding ion motion and causing the observed NDR. Furthermore, we expect the same mechanism to operate in the negative electric field regime as well. However, the *I-E* curves show that NDR originates at a higher applied electric field in the negative regime. This phenomenon can be explained by the presence of an intrinsic electric field inside the nanopore, due to the Janus nature of the membrane. As shown in Figure 1, the membrane has molybdenum sandwiched between sulfur (more electronegative) on

the right and selenium (less electronegative) on the left. This results in an intrinsic electric field in the nanopore directed parallel to the applied field (strengthening it) for positive biases and antiparallel to the applied field (weakening it) for negative biases. As a result of this weakening of field for negative biases, NDR is observed at a higher magnitude of applied electric field.

3.2 Origin of hysteresis

Figures 2B,C show that the water orientation distributions are narrower (smaller standard deviation) in the reverse sweep, compared to the forward sweep. This explains the lower currents in the reverse sweep, where hysteresis in the water structure leads to a more oriented configuration compared to forward sweep. As explained in the previous section, this oriented water structure increases the ion translocation barrier, thereby impeding ion motion and reducing flux. To further understand the origin of this hysteresis in water structure, we looked at the dynamics of this water structure orientation process and extracted the associated timescales as a function of electric field in the forward and reverse sweeps, as shown in Figure 2D. Figure 3 shows the forward and reverse orientation processes in time, where we start from a relaxed system and gradually increase the electric field in the forward process (Figure 3A) and reduce the field in the reverse process (Figure 3B). Here, "σ_θ" is the standard deviation of the water orientation distribution at each timestep. The plots show that in the forward sweep, as the applied field is increased, there is an exponential decrease in σ_θ, whereas in the reverse sweep, as the field is decreased, there is an exponential increase in σ_θ. We extracted the timescales "τ" shown
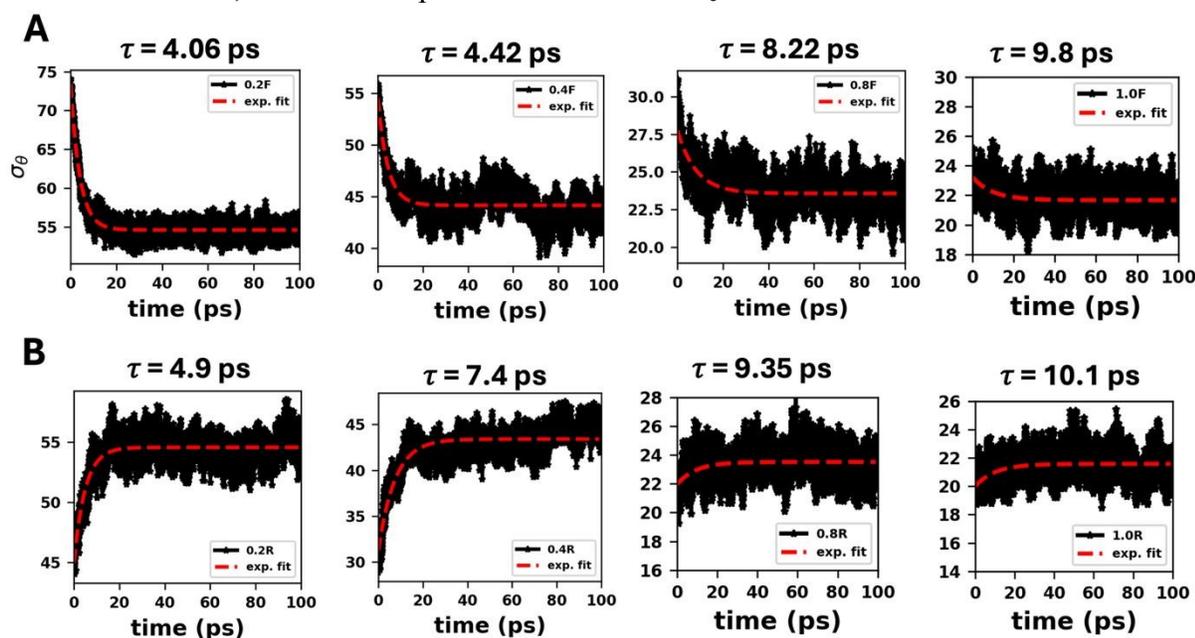
Figure 3 standard deviation of the water orientation distributions as a function of time for different electric fields in (A) forward and (B) reverse sweeps. Here τ is the timescale extracted from the exponential fit.

in Figure 2D, by fitting $\sigma_\theta = A + Be^{-t/\tau}$ in the forward sweep and $\sigma_\theta = A + B(1 - e^{-t/\tau})$ in the reverse sweep. These timescales show that in the forward sweep, the water orientation process happens on faster timescales compared to the relaxation process indicating that the system holds memory in the form of oriented water structure. This explains the narrower water orientation distributions in the reverse sweep compared to the forward sweep (Figure 2B,C) and the hysteresis in the ionic current.
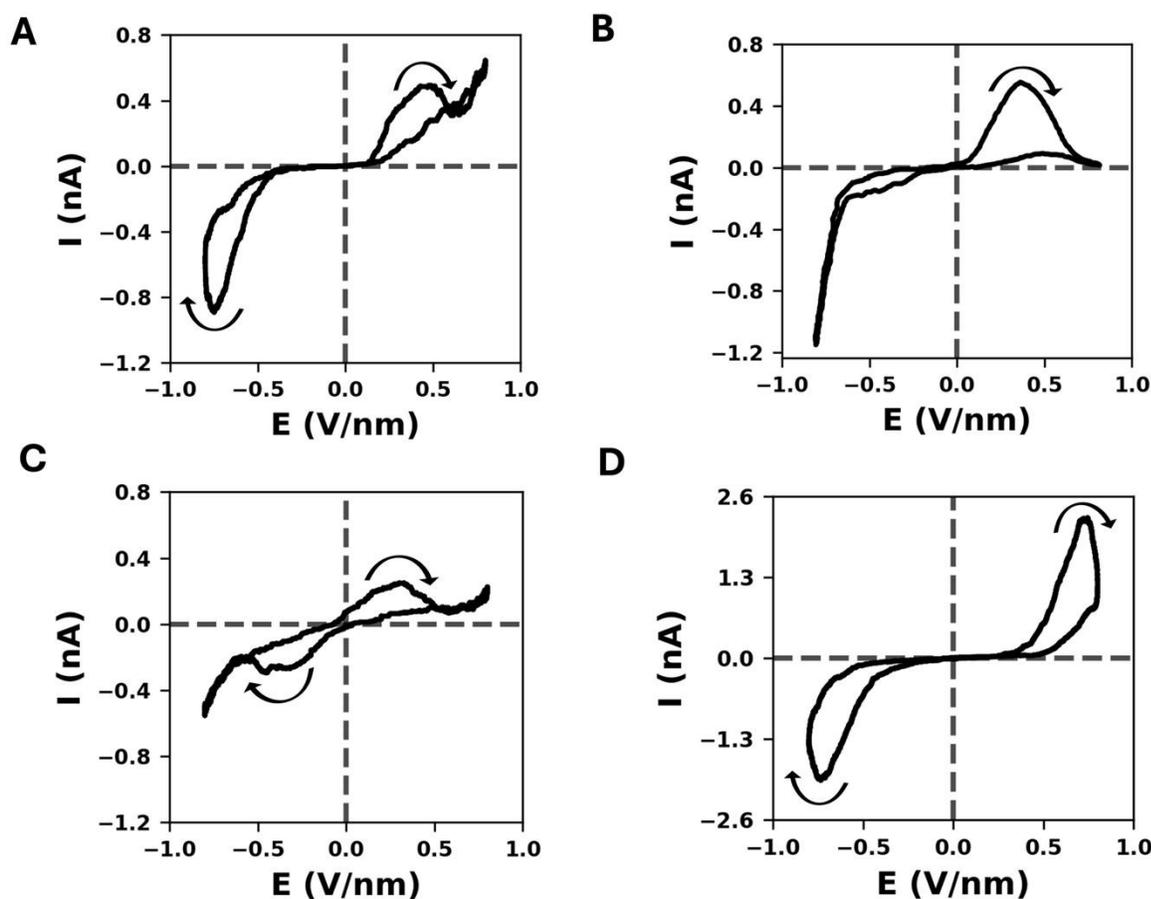

Figure 4 *I-E* curves for different systems with (A) Se = -0.53e, Mo = 1.06e, S = -0.53e, (B) Se = -0.35e, Mo = 1.06e, S = -0.71e, (C) Se = 0e, Mo = 0e, S = 0e, as the membrane charges. (D) *I-E* curves for MoS_2 system with Mo = 1.18e, S = -0.59e as the membrane charges.

Overall, the mechanism of NDR and hysteresis can be described as follows – as the electric field increases, the water molecules inside the nanopore become more oriented, with their dipoles pointing along the applied field direction. This reorientation leads to a larger Cl⁻ translocation energy barrier as the electric field is increased, causing the NDR. During the reverse sweep, as the electric field decreases, the ordered water structure relaxes on a longer timescale compared to the forward process. This delayed relaxation results in a narrower water distribution, higher Cl⁻ ion translocation barriers, and lower currents during the reverse sweep,

leading to the observed *I-E* hysteresis. Furthermore, the intrinsic field of the membrane in the nanopore causes the NDR to occur at a higher applied electric field magnitude in the negative field regime. Finally, to confirm that the NDR and hysteresis originate from the water structure rather than the membrane charges, we repeated the calculations using membranes with modified S and Se charges to impose higher or lower charge asymmetry (Figure 4). We also examined a fictitious charge neutral membrane (Figure 4C) and MoS_2 (Figure 4D). In all cases, NDR and hysteresis persisted, reinforcing that both phenomena arise from the water structure inside the nanopore, with the Janus nature of the membrane enhancing these phenomena.
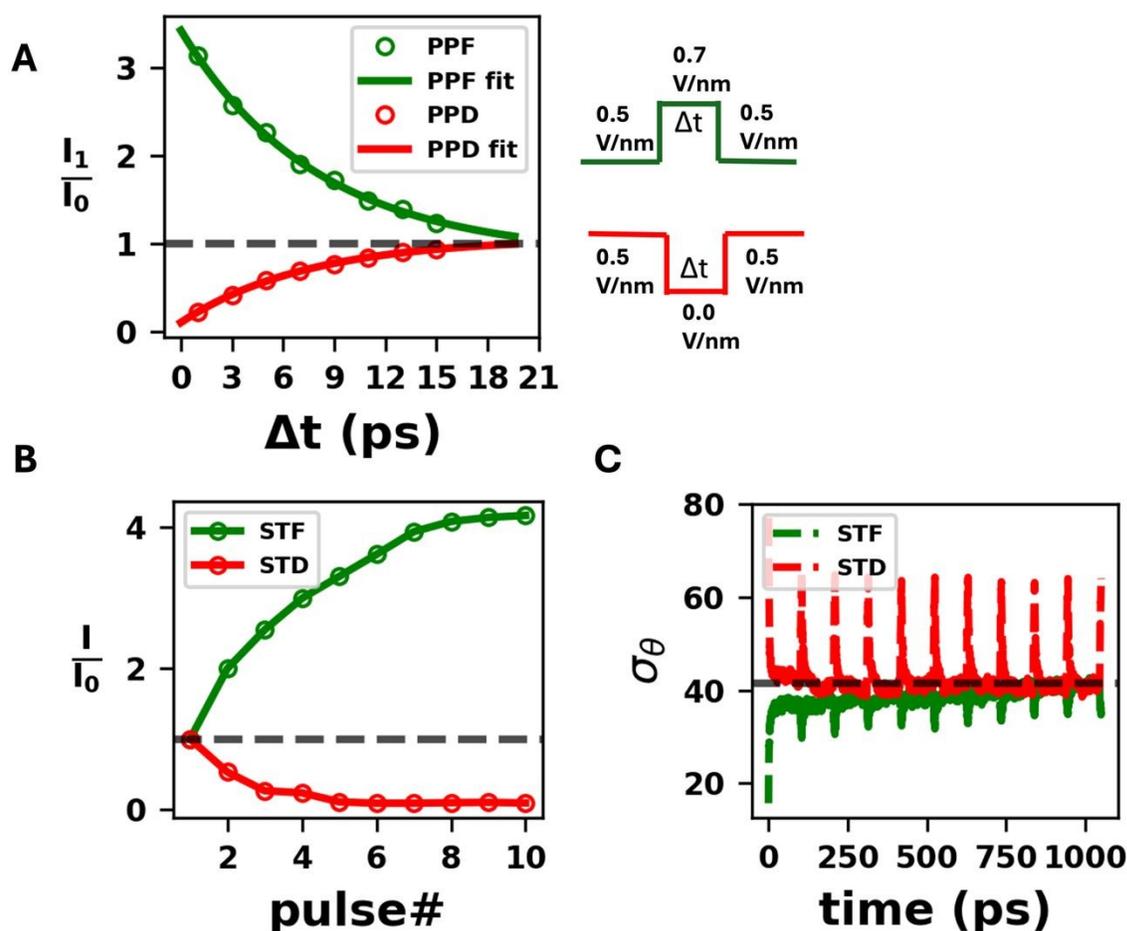
Figure 5 (A) PPF and PPD plots along with the exponential fits, (B) STF and STD plots using *Δt* = 5ps, (C) Standard deviation of the water orientation distributions as a function of time during STF/STD simulations.

3.3 Emulating Synaptic functions

One of the key features exhibited by synapses between biological neurons that enables information processing and short-term memory is short-term plasticity (STP). This short-term synaptic plasticity is governed by a finite memory timescale of the synapse, which dictates how

long the influence of a preceding signal persists. To demonstrate an analogous behavior in our system and to quantify this memory timescale, we performed paired-pulse facilitation (PPF) and paired-pulse depression (PPD) computations, by applying two electric field pulses with a variable delay time (Δt) in between. The ratio of the second pulse current to first pulse current (I_1/I_0) can be used to demonstrate facilitation or depression phenomena exhibited by biological synapses.

For PPF, starting from a highly oriented water configuration (generated by applying 2.0 V/nm for 20 ps), electric field pulses of 0.7V/nm were applied with a delay period where 0.5V/nm was applied. For PPD, starting from a relaxed system (at 0 V/nm), electric field pulses of 0.5V/nm were applied with a delay period where no electric field was applied. Figure 5A shows the facilitation in current which decays exponentially from I_1/I_0 = *3.1 to 1.2* for PPF and depression in current which grows exponentially from I_1/I_0 = *0.2 to 0.9* for PPD. Further, we extracted the memory timescales by fitting exponential functions $\frac{I_1}{I_0} = A_0 + A_1 \exp\left(-\frac{\Delta t}{\tau_f}\right)$ to the facilitation curve and $\frac{I_1}{I_0} = A_0 + A_1\left(1 - \exp\left(-\frac{\Delta t}{\tau_d}\right)\right)$ to the depression curve. We extracted "τ_f = 8ps" and "τ_d=7.5ps" as the respective memory timescales for the facilitation and depression processes in our system, indicating that the nanopore retains memory of the preceding field stimulus over a few picoseconds.

Having established τ = 7-8ps as the intrinsic relaxation time of our system, we investigated short-term facilitation (STF) and short-term depression (STD) using multiple pulses with a delay time between the pulses. Here, the delay time was chosen as Δt = 5ps < τ. In this regime, the memory of the previous pulse is not fully erased before the next one arrives, allowing cumulative plasticity to emerge. Figure 5B shows both STF and STD behaviors exhibited by our system. For STF, we can see that the normalized current (I_n/I_0) increases over successive cycles, saturating at ~4 after 10 pulses. For STD, we can see the normalized current slowly decay to zero over successive pulses. Furthermore, to directly show the analogous behavior to facilitation or depression in synaptic efficacy in biological neurons, we probed the nanopore conductance as a function of time as the pulse trains are applied. Here, we used the standard deviation of the water dipole orientation distribution functions (σ_θ) as a proxy for nanopore conductance. Figure 5C shows increase in this standard deviation (and nanopore conductance) with successive pulses during facilitation and decrease in standard deviation (and nanopore conductance) during depression.

Together, the PPF/PPD relaxation analysis and the STF/STD pulse-train results reveal a coherent picture: the sub-nanometer pore system exhibits short-term plasticity when operated in the Δt < 8ps regime, where successive input signals interact through residual water orientational order, enabling both facilitation and depression analogous to biological synapses. This showcases the ability of our system to emulate key hallmarks of short-term synaptic plasticity, enabling its application in neuromorphic computing. Furthermore, while the memory time scales

exhibited by our system are shorter than those typically accessible experimentally, the underlying mechanism reported here is not restricted to these time scales. The characteristic response time associated with solvent alignment depends on system parameters such as pore dimensions and properties, solvent properties, and the magnitude of the applied field. In particular, lower driving voltages, or the use of heavier polar solvents with slower dynamics[9] are expected to shift the time scales of solvent alignment induced negative differential resistance and hysteresis to longer, experimentally accessible values.

4. Conclusions

In this work, we demonstrated that a single angstrom MoSSe pore exhibits memristive behavior and negative differential resistance (NDR) arising from the dynamic coupling between confined water structure and ionic transport. Molecular dynamics simulations under oscillating electric fields revealed a pinched loop hysteresis in the current–electric field (I–E) characteristics and a distinct NDR region. Further analysis showed that these nonlinear transport features originate from field induced ordering of water dipoles within the nanopore, which modifies the ion–water interaction energy landscape and reduces ion mobility causing NDR. Furthermore, the delayed relaxation of this ordered water structure in the reverse sweep compared to the forward sweep leads to current hysteresis, representing the emergence of memristive behavior. The same mechanism also enables emulation of synaptic plasticity observed in biological neurons. Sequential electric field pulses produced facilitation and depression, where the nanopore conductance evolved according to the history of applied pulses. Paired pulse computations further revealed exponential relaxation kinetics, with the relaxation times (order of few picoseconds) defining the intrinsic memory timescales of the device. Together, these findings establish that solvent dipole ordering and relaxation can serve as the physical origin for achieving non-linear ion transport behaviors like NDR and current hysteresis. More broadly, this study suggests that control of solvent order and ion–solvent coupling at the angstrom scale can enable a new class of iontronic nanofluidic memristors for neuromorphic computing applications.

Author contributions

Conceptualization: MTD, NA; Methodology: MTD, NA; Formal analysis: MTD; Investigation: MTD; Writing-Original Draft: MTD; Writing-Review & Editing: NA; Supervision: NA.

Conflicts of interest

There are no conflicts of interest to declare.

Acknowledgement

References

(1)   RAMON Y CAJAL, D. S. NUEVA CONCEPTA DE LA HISTOLOGIA DE LOS CENTROS NERVOSOS. *Ann Surg* 1893, *18*.

(2)   Jo, S. H.; Chang, T.; Ebong, I.; Bhadviya, B. B.; Mazumder, P.; Lu, W. Nanoscale Memristor Device as Synapse in Neuromorphic Systems. *Nano Lett* 2010, *10* (4), 1297–1301. https://doi.org/10.1021/nl904092h.

(3)   Chua, L. Memristor-The Missing Circuit Element. *IEEE Transactions on Circuit Theory* 1971, *18* (5), 507–519. https://doi.org/10.1109/TCT.1971.1083337.

(4)   Strukov, D. B.; Snider, G. S.; Stewart, D. R.; Williams, R. S. The Missing Memristor Found. *Nature* 2008, *453* (7191), 80–83. https://doi.org/10.1038/nature06932.

(5)   Pershin, Yu. V; Di Ventra, M. Spin Memristive Systems: Spin Memory Effects in Semiconductor Spintronics. *Phys Rev B* 2008, *78* (11), 113309. https://doi.org/10.1103/PhysRevB.78.113309.

(6)   Driscoll, T.; Kim, H.-T.; Chae, B.-G.; Di Ventra, M.; Basov, D. N. Phase-Transition Driven Memristive System. *Appl Phys Lett* 2009, *95* (4), 043503. https://doi.org/10.1063/1.3187531.

(7)   Chanthbouala, A.; Garcia, V.; Cherifi, R. O.; Bouzehouane, K.; Fusil, S.; Moya, X.; Xavier, S.; Yamada, H.; Deranlot, C.; Mathur, N. D.; Bibes, M.; Barthélémy, A.; Grollier, J. A Ferroelectric Memristor. *Nat Mater* 2012, *11* (10), 860–864. https://doi.org/10.1038/nmat3415.

(8)   Ge, R.; Wu, X.; Kim, M.; Shi, J.; Sonde, S.; Tao, L.; Zhang, Y.; Lee, J. C.; Akinwande, D. Atomristor: Nonvolatile Resistance Switching in Atomic Sheets of Transition Metal Dichalcogenides. *Nano Lett* 2018, *18* (1), 434–441. https://doi.org/10.1021/acs.nanolett.7b04342.

(9)   Dronadula, M. T.; Aluru, N. R. Solvent Structure and Dynamics Controlled Memristive Ion Transport in Å-Scale Channels. *J Phys Chem Lett* 2026, *17* (1), 127–133. https://doi.org/10.1021/acs.jpclett.5c03397.

(10)   Powell, M. R.; Cleary, L.; Davenport, M.; Shea, K. J.; Siwy, Z. S. Electric-Field-Induced Wetting and Dewetting in Single Hydrophobic Nanopores. *Nat Nanotechnol* 2011, *6* (12), 798–802. https://doi.org/10.1038/nnano.2011.189.

(11)   Wang, D.; Kvetny, M.; Liu, J.; Brown, W.; Li, Y.; Wang, G. Transmembrane Potential across Single Conical Nanopores and Resulting Memristive and Memcapacitive Ion Transport. *J Am Chem Soc* 2012, *134* (8), 3651–3654. https://doi.org/10.1021/ja211142e.

Faraday Discussions Accepted Manuscript

(12)   Bu, Y.; Ahmed, Z.; Yobas, L. A Nanofluidic Memristor Based on Ion Concentration Polarization. *Analyst* 2019, *144* (24), 7168–7172. https://doi.org/10.1039/C9AN01561B.

(13)   Xiong, T.; Li, C.; He, X.; Xie, B.; Zong, J.; Jiang, Y.; Ma, W.; Wu, F.; Fei, J.; Yu, P.; Mao, L. Neuromorphic Functions with a Polyelectrolyte-Confined Fluidic Memristor. *Science (1979)* 2023, *379* (6628), 156–161. https://doi.org/10.1126/science.adc9150.

(14)   Song, R.; Wang, P.; Zeng, H.; Zhang, S.; Wu, N.; Liu, Y.; Zhang, P.; Xue, G.; Tong, J.; Li, B.; Ye, H.; Liu, K.; Wang, W.; Wang, L. Nanofluidic Memristive Transition and Synaptic Emulation in Atomically Thin Pores. *Nano Lett* 2025, *25* (14), 5646–5655. https://doi.org/10.1021/acs.nanolett.4c06297.

(15)   Robin, P.; Kavokine, N.; Bocquet, L. Modeling of Emergent Memory and Voltage Spiking in Ionic Transport through Angstrom-Scale Slits. *Science (1979)* 2021, *373* (6555), 687–691. https://doi.org/10.1126/science.abf7923.

(16)   Robin, P.; Emmerich, T.; Ismail, A.; Niguès, A.; You, Y.; Nam, G.-H.; Keerthi, A.; Siria, A.; Geim, A. K.; Radha, B.; Bocquet, L. Long-Term Memory and Synapse-like Dynamics in Two-Dimensional Nanofluidic Channels. *Science (1979)* 2023, *379* (6628), 161–167. https://doi.org/10.1126/science.adc9931.

(17)   Li, Z.; Myers, S. K.; Xiao, J.; Li, Y.; Noy, N.; Leuski, A.; Noy, A. Neuromorphic Ionic Computing in Droplet Interface Synapses. *Sci Adv* 2025, *11* (30), eadv6603. https://doi.org/10.1126/sciadv.adv6603.

(18)   Ismail, A.; Nam, G.-H.; Lokhandwala, A.; Pandey, S. V.; Saurav, K. V.; You, Y.; Jyothilal, H.; Goutham, S.; Sajja, R.; Keerthi, A.; Radha, B. Programmable Memristors with Two-Dimensional Nanofluidic Channels. *Nat Commun* 2025, *16* (1), 7008. https://doi.org/10.1038/s41467-025-61649-6.

(19)   FitzHugh, R. Impulses and Physiological States in Theoretical Models of Nerve Membrane. *Biophys J* 1961, *1* (6), 445–466. https://doi.org/https://doi.org/10.1016/S0006-3495(61)86902-6.

(20)   Nagumo, J.; Arimoto, S.; Yoshizawa, S. An Active Pulse Transmission Line Simulating Nerve Axon. *Proceedings of the IRE* 1962, *50* (10), 2061–2070. https://doi.org/10.1109/JRPROC.1962.288235.

(21)   Ahsan, R.; Wu, Z.; Jalal, S. A. A.; Kapadia, R. Ultralow Power Electronic Analog of a Biological Fitzhugh–Nagumo Neuron. *ACS Omega* 2024, *9* (16), 18062–18071. https://doi.org/10.1021/acsomega.3c09936.

(22)   Pickett, M. D.; Medeiros-Ribeiro, G.; Williams, R. S. A Scalable Neuristor Built with Mott Memristors. *Nat Mater* 2013, *12* (2), 114–117. https://doi.org/10.1038/nmat3510.

(23)   Pei, Y.; Yang, B.; Zhang, X.; He, H.; Sun, Y.; Zhao, J.; Chen, P.; Wang, Z.; Sun, N.; Liang, S.; Gu, G.; Liu, Q.; Li, S.; Yan, X. Ultra Robust Negative Differential Resistance Memristor for Hardware Neuron Circuit Implementation. *Nat Commun* 2025, *16* (1), 48. https://doi.org/10.1038/s41467-024-55293-9.

(24)   Jacob, B.; Silva, J.; Figueiredo, J. M. L.; Nieder, J. B.; Romeira, B. Light-Induced Negative Differential Resistance and Neural Oscillations in Neuromorphic Photonic Semiconductor Micropillar Sensory Neurons. *Sci Rep* 2025, *15* (1), 6805. https://doi.org/10.1038/s41598-025-90265-z.

(25)   Ma, Y.; Niu, Y.; Pei, R.; Wang, W.; Wei, B.; Xie, Y. Reconfigurable Neuromorphic Computing by a Microdroplet. *Cell Rep Phys Sci* 2024, *5* (9). https://doi.org/10.1016/j.xcrp.2024.102202.

(26)   Yang, R.; Balogun, Y.; Ake, S.; Baram, D.; Brown, W.; Wang, G. Negative Differential Resistance in Conical Nanopore Iontronic Memristors. *J Am Chem Soc* 2024, *146* (19), 13183–13190. https://doi.org/10.1021/jacs.4c00922.

(27)   Berendsen, H. J. C.; van der Spoel, D.; van Drunen, R. GROMACS: A Message-Passing Parallel Molecular Dynamics Implementation. *Comput Phys Commun* 1995, *91* (1), 43–56. https://doi.org/https://doi.org/10.1016/0010-4655(95)00042-E.

(28)   Hess, B.; Kutzner, C.; van der Spoel, D.; Lindahl, E. GROMACS 4: Algorithms for Highly Efficient, Load-Balanced, and Scalable Molecular Simulation. *J Chem Theory Comput* 2008, *4* (3), 435–447. https://doi.org/10.1021/ct700301q.

(29)   Pronk, S.; Páll, S.; Schulz, R.; Larsson, P.; Bjelkmar, P.; Apostolov, R.; Shirts, M. R.; Smith, J. C.; Kasson, P. M.; van der Spoel, D.; Hess, B.; Lindahl, E. GROMACS 4.5: A High-Throughput and Highly Parallel Open Source Molecular Simulation Toolkit. *Bioinformatics* 2013, *29* (7), 845–854. https://doi.org/10.1093/bioinformatics/btt055.

(30)   Abraham, M. J.; Murtola, T.; Schulz, R.; Páll, S.; Smith, J. C.; Hess, B.; Lindahl, E. GROMACS: High Performance Molecular Simulations through Multi-Level Parallelism from Laptops to Supercomputers. *SoftwareX* 2015, *1–2*, 19–25. https://doi.org/https://doi.org/10.1016/j.softx.2015.06.001.

(31)   Nosé, S. A Unified Formulation of the Constant Temperature Molecular Dynamics Methods. *J Chem Phys* 1984, *81* (1), 511–519. https://doi.org/10.1063/1.447334.

(32)   Hoover, W. G. Canonical Dynamics: Equilibrium Phase-Space Distributions. *Phys Rev A (Coll Park)* 1985, *31* (3), 1695–1697. https://doi.org/10.1103/PhysRevA.31.1695.

(33)   Darden, T.; York, D.; Pedersen, L. Particle Mesh Ewald: An N Log (N) Method for Ewald Sums in Large Systems. *Journal of chemical physics* 1993, *98*, 10089.

(34)   Berendsen, H. J. C.; Grigera, J.-R.; Straatsma, T. P. The Missing Term in Effective Pair Potentials. *Journal of Physical Chemistry* 1987, *91* (24), 6269–6271.

(35)   Joung, I. S.; Cheatham, T. E. I. I. I. Molecular Dynamics Simulations of the Dynamic and Energetic Properties of Alkali and Halide Ions Using Water-Model-Specific Ion Parameters. *J Phys Chem B* 2009, *113* (40), 13279–13290. https://doi.org/10.1021/jp902584c.

(36)   Liang, T.; Phillpot, S. R.; Sinnott, S. B. Parametrization of a Reactive Many-Body Potential for Mo--S Systems. *Phys Rev B* 2009, *79* (24), 245110. https://doi.org/10.1103/PhysRevB.79.245110.

(37)   Best, R. B.; Zhu, X.; Shim, J.; Lopes, P. E. M.; Mittal, J.; Feig, M.; MacKerell, A. D. Jr. Optimization of the Additive CHARMM All-Atom Protein Force Field Targeting Improved Sampling of the Backbone ϕ, ψ and Side-Chain X1 and X2 Dihedral Angles. *J Chem Theory Comput* 2012, *8* (9), 3257–3273. https://doi.org/10.1021/ct300400x.

(38)   Henkelman, G.; Arnaldsson, A.; Jónsson, H. A Fast and Robust Algorithm for Bader Decomposition of Charge Density. *Comput Mater Sci* 2006, *36* (3), 354–360. https://doi.org/https://doi.org/10.1016/j.commatsci.2005.04.010.

(39)   Wang, M.; Wang, X.; Zheng, M.; Zhou, X. Improving Catalytic Activity of "Janus" MoSSe Based on Surface Interface Regulation. *Molecules* 2022, *27* (18), 6038.

(40)   Güller, F.; Llois, A. M.; Goniakowski, J.; Noguera, C. Prediction of Structural and Metal-to-Semiconductor Phase Transitions in Nanoscale ${\mathrm{MoS}}_{2}$, ${\mathrm{WS}}_{2}$, and Other Transition Metal Dichalcogenide Zigzag Ribbons. *Phys Rev B* 2015, *91* (7), 75407. https://doi.org/10.1103/PhysRevB.91.075407.

(41)   Dzubiella, J.; Hansen, J.-P. Electric-Field-Controlled Water and Ion Permeation of a Hydrophobic Nanopore. *J Chem Phys* 2005, *122* (23), 234706. https://doi.org/10.1063/1.1927514.

Data Availability Statement

All the data presented in the manuscript is available from the authors upon request.

Faraday Discussions Accepted Manuscript